Supplemental Information

Whole-Brain Neuronal Activity Displays

Crackling Noise Dynamics

Adrián Ponce-Alvarez, Adrien Jouary, Martin Privat, Gustavo Deco, and Germán Sumbre

Supplemental Information

Inventory

Supplementary tables, figures, and videos

Supplementary tables

Dataset #	Ca²⁺ indicator	Nb. of ROIs	Q	ρ_c	$P(C_s) \sim C_s^{-\sigma}$				$g(r) \sim r^{-\eta}$	
					KS stat.	$\sigma(\rho_c)$	cutoffs	LLR (norm.)	η	cutoffs
1	GCAMP5	41,115	9	0.24	0.036	2.17 ± 0.01	[6, 10³]	+55.2*	0.16 ± 0.01	[10, 500]
2	GCAMP6f	84,177	6	0.16	0.031	2.16 ± 0.01	[6, 10³]	+72.1*	0.24 ± 0.01	[10, 500]
3	GCAMP6f	86,110	6	0.11	0.021	2.22 ± 0.01	[6, 10³]	+113.5*	0.22 ± 0.01	[10, 500]
4	GCAMP6f	89,349	3	0.08	0.041	2.20 ± 0.01	[6, 10³]	+75.88*	0.14 ± 0.01	[10, 500]
5	GCAMP5	51,466	8	0.15	0.043	1.97 ± 0.01	[6, 10³]	+112.6*	0.27 ± 0.01	[10, 500]
6	GCAMP5	50,731	5	0.14	0.046	2.15 ± 0.01	[6, 10³]	+70.5*	0.23 ± 0.01	[10, 500]

Table S1. Summary of the statistics of the spatial clusters for each dataset. Related to Figure 1. Q: number of spontaneous and stimulus segments (20 min of spontaneous activity and 4 min of visual stimulation). ρ_c: fraction of activated ROIs that maximizes the average number of connected components ($\langle m \rangle$). The probability of cluster sizes C_s was evaluated for the set of clusters with ρ comprised between $\rho_c - \Delta$ and $\rho_c + \Delta$, where Δ=0.02, and for $C_{s,\min} \leq C_s \leq C_{s,\max}$ (cutoffs). The probability density was fitted to a truncated power law using MLE (Marshall et al., 2016). In the table, we reported the MLE power exponent $\sigma(\rho_c)$ (± the estimation error), the KS-statistics between the data distribution and the fitted MLE power law, and the cutoffs $[C_{s,\min}, C_{s,\max}]$. We also reported the normalized log-likelihood ratio (LLR) for the comparison between the power-law and the log-normal distributions. Significantly positive values of LLR indicate that the power-law distribution was a better predictor of the data than the log-normal distribution; asterisks indicate that LLR were statistically different from zero (p < 0.001). Finally, we calculated the correlation function $g(r)$, i.e., the average correlation between pairs of ROIs as a function of the Euclidean distance between them (r). We fitted the relation $g(r) \sim r^{-\eta}$ using least squares for $r_{\min} \leq r \leq r_{\max}$ (cutoffs, in μm) and obtained the exponent η and its estimation error.

Data-set	$P(T)\sim T^{-\alpha}$				$P(S)\sim S^{-\tau}$				$\langle S\rangle(T)\sim T^{1/\sigma\nu z}$	Profile collapse		Recurrence-time collapse	
	KS stat.	α	cutoffs	LLR	KS stat.	τ	cutoffs	LLR	$\sigma\nu z$	$\sigma\nu z$	$\Delta\sigma_F^2$	γ	$\Delta\sigma_G^2$
1	0.015	2.86 ± 0.01	[1.88, 18.8]	+192.3*	0.022	2.10 ± 0.01	[6; 10^4]	+99.9*	0.52 ± 0.02	0.55	3.8	0.17	4.6
2	0.007	2.92 ± 0.02	[2.35, 18.8]	+23.1*	0.035	2.01 ± 0.01	[6; 2×10^4]	+35.5*	0.59 ± 0.02	0.60	10.1	0.45	5.7
3	0.008	3.44 ± 0.01	[0.94, 18.8]	+172.5*	0.046	1.98 ± 0.01	[6; 2×10^4]	+27.2*	0.51 ± 0.02	0.51	10.5	0.43	4.5
4	0.013	3.22 ± 0.03	[2.82, 18.8]	+5.9*	0.039	2.06 ± 0.01	[6; 2×10^4]	+41.8*	0.55 ± 0.03	0.56	3.9	0.37	1.9
5	0.018	2.72 ± 0.01	[1.41, 18.8]	+69.0*	0.024	1.96 ± 0.01	[6; 10^4]	+30.7*	0.52 ± 0.01	0.54	12.5	0.23	4.2
6	0.013	2.90 ± 0.02	[2.35, 18.8]	+46.4*	0.026	1.91 ± 0.01	[6; 10^4]	+77.83*	0.53 ± 0.02	0.53	8.8	0.33	5.6
7	0.017	2.25 ± 0.02	[1.41, 18.8]	+36.9*	0.018	1.64 ± 0.01	[6; 10^4]	+32.6*	0.57 ± 0.03	0.65	2.8	0.30	2.6
8	0.028	2.07 ± 0.02	[1.41, 18.8]	+5.2*	0.041	1.73 ± 0.002	[6; 10^4]	-1.5[n.s.]	0.68 ± 0.02	0.67	2.6	0.86	0.7

Table S2. Summary of the statistics of the neuronal avalanches for each dataset. Related to Figure 2; Figure 3; Figure 5. We evaluated the probability distribution of avalanche durations T and sizes S. For each distribution, we fitted truncated power laws using MLE ($P(T)\sim T^{-\alpha}$ and $P(S)\sim S^{-\tau}$) and further evaluated the fitting using KS-statistics. The estimation error of the MLE power exponent was calculated using bootstrap re-sampling. The cutoffs ($T \in [T_{\min}, T_{\max}]$ and $S \in [S_{\min}, S_{\max}]$) of the truncated power laws are also indicated. We also reported the normalized log-likelihood ratio (LLR) for the comparison between the power-law and the log-normal distributions. Significantly positive values of LLR indicate that the power-law distribution was a better predictor of the data than the log-normal distribution; asterisks indicate that LLR were statistically different from zero (p < 0.001). We also calculated the average size $\langle S\rangle(T)$ of avalanches of duration T and fit the relation $\langle S\rangle(T)\sim T^{-1/\sigma\nu z}$ using least squares (within the corresponding duration and size cutoffs) to obtain the exponent $\sigma\nu z$ and its estimation error. We estimated the best possible collapse of the avalanche profiles given by: $\langle S(t,T)\rangle T^{1-1/\sigma\nu z} = F(t/T)$. The exponent $\sigma\nu z$ was estimated using the method of Marshall et al. (2016). $\Delta\sigma_F^2$: amount of collapse. The curve onto which the scaled recurrence time distributions collapse was approximated by a gamma distribution with the shape parameter given by γ. The amount of collapse was evaluated by $\Delta\sigma_G^2$. Datasets 7 and 8 correspond to larvae exposed to heptanol before the experiments.
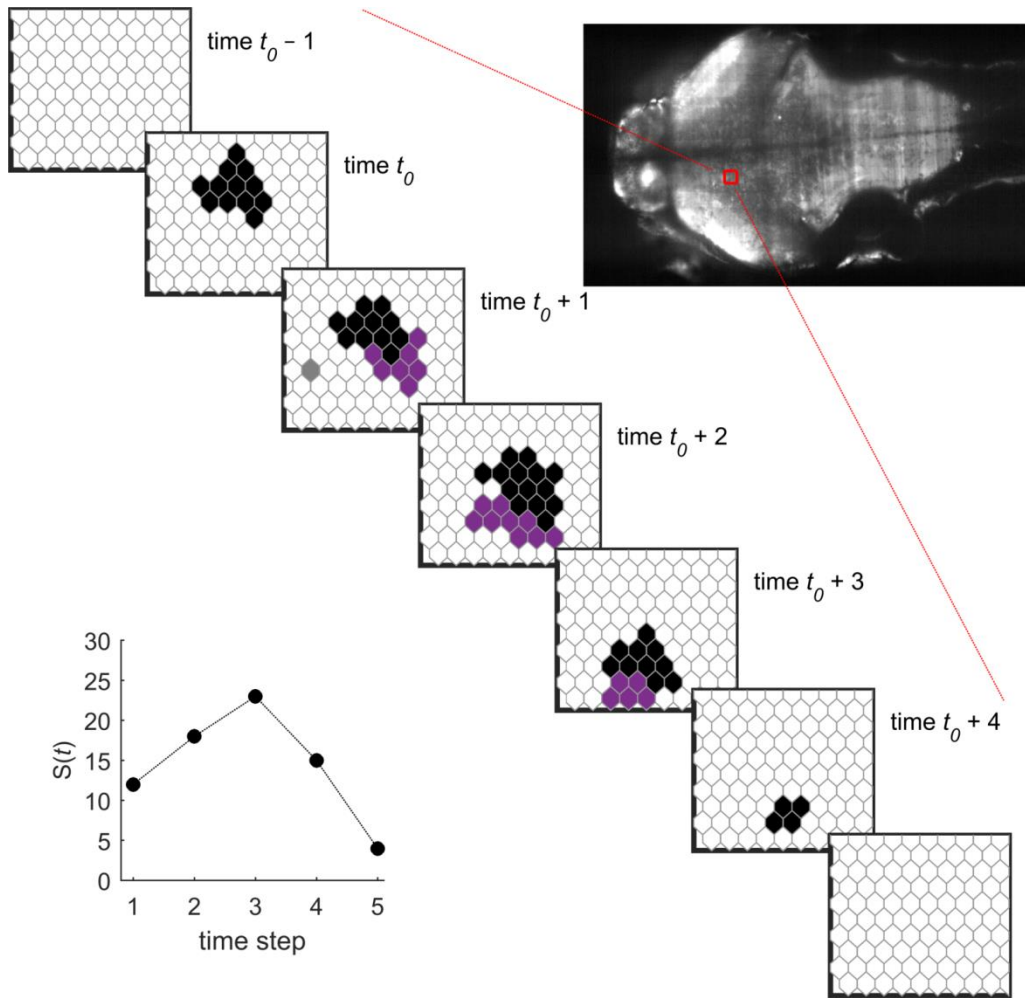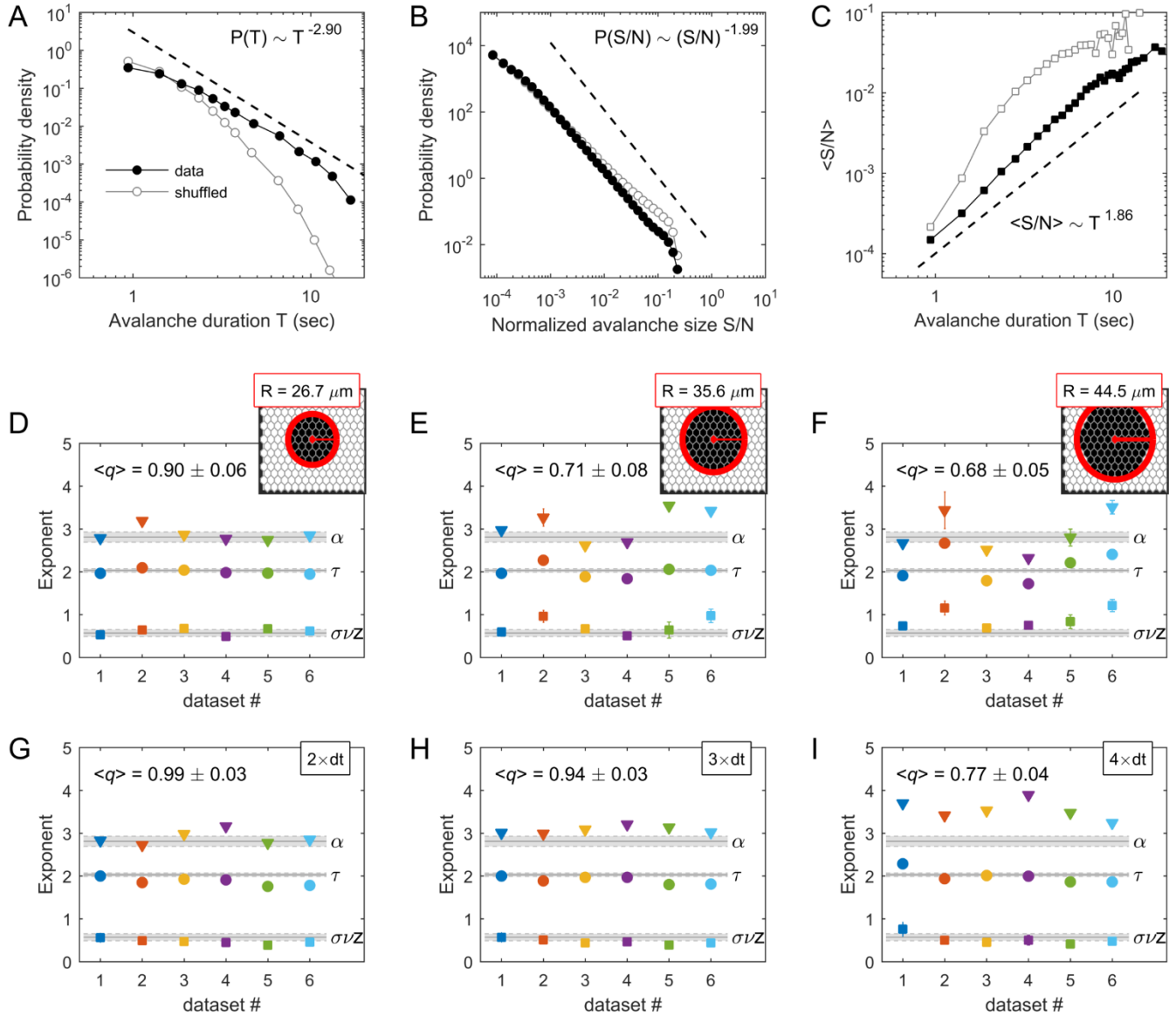
Supplementary figures

Supplemental figure S1. Selective-plane illumination microscopy (SPIM). Related to Methods: *Selective-plane illumination microscopy*. **A**: Scheme of the optical path of the light-sheet microscope. **B**: Subset of coronal sections obtained with the SPIM. The full stack corresponds to 40 coronal sections recorded every 5 µm. In each coronal section, a hexagonal grid was applied to obtain the ROIs from which the average fluorescence signal was extracted. **C.** The relative increase in fluorescence intensity ($\Delta F/F$) of five example ROIs. *Left*: location of the ROIs. *Right*: fluorescence intensity for the example ROIs; Ca^{+2} transients that exceed the binarization threshold are shown in red. **D:** Experimental paradigm. The experiment was composed of Q consecutive segments of 20 min of spontaneous activity and 4 min of visual stimulation. Q was different for different datasets and ranges between 3–9 (see **Table S1**). *Inset*: Each visual stimulation period contained 8 sub-episodes during which a moving grating was presented below the larva for 10 sec (represented in gray). The motion directions of the 8 gratings were equal to 0°, 60°, 180°, -60°, 0°, 60°, 180°, and -60°, respectively, relative to the larva's caudo-rostral axis. The inter-stimulus interval was equal to 20 sec.
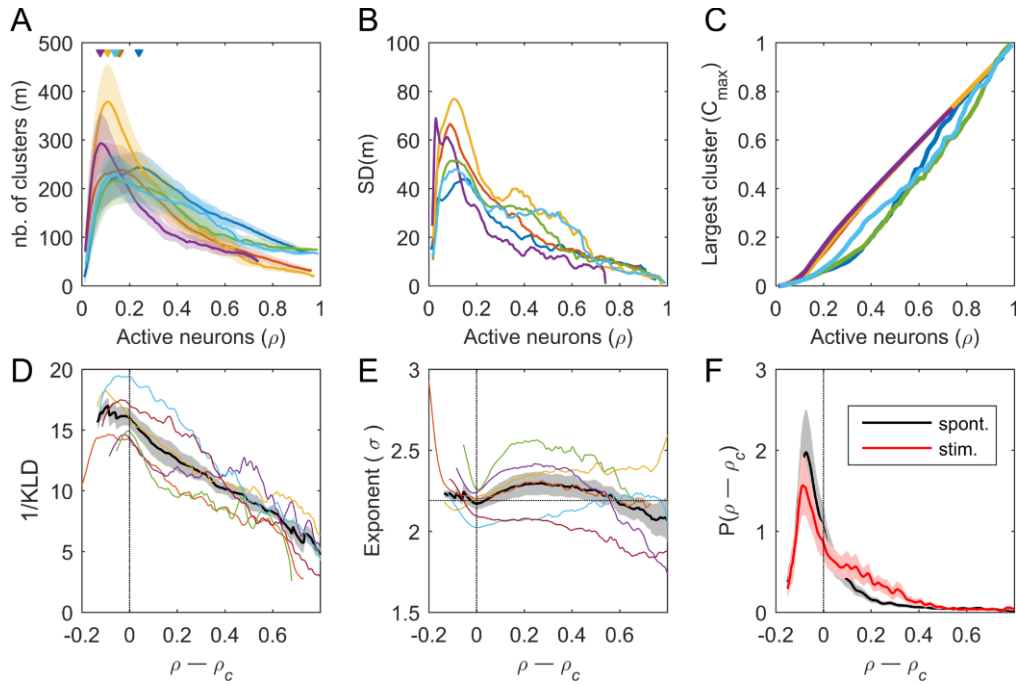
Supplemental figure S2. Spatial clusters. Related to Figure 1. A-B: Number of activity clusters (*m*) as a function of the proportion of active ROIs (ρ) for each dataset (color traces). In panel (A) the shaded areas represent standard deviation of *m*, which is represented in (B) as a function of ρ. **C:** Normalized size of the largest cluster (*C_max*) as a function of ρ. **D-E:** The cluster size distribution for the set of clusters that appeared with *p* comprised within small intervals [ρ − Δ; ρ + Δ] with Δ=0.02 was fitted to a power law. The goodness-of-fit (1/KLD) of the power law (D) and the estimated power exponent (E) were calculated as a function of $\rho - \rho_c$, for each dataset (color traces). The black traces represent the average goodness-of-fit and the average power exponent. The gray areas represent SEM. **F:** Distribution of $\rho - \rho_c$ (*black*: spontaneous activity, *red*: for stimulus-evoked activity) averaged over all datasets (the mean and the SEM of the distributions are indicated by the solid line and the shaded area, respectively).
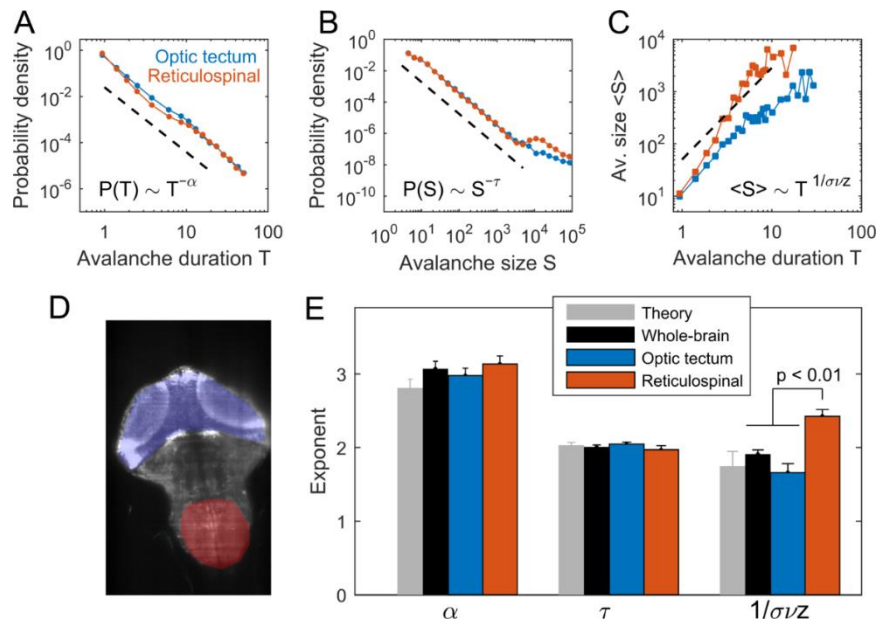
Supplemental figure S3. Avalanche definition. Related to Figure 2. The illustration of an avalanche is shown here in 2D for simplicity but note that the analysis was done in 3D. An avalanche was initiated with the detection of a cluster of active ROIs at time t_0, the avalanche continued at time t_0+1 with a cluster composed of ROIs that were active at the preceding time t_0 (represented in black) plus ROIs that activated at t_0+1 (represented in purple), and so on, until this condition no longer held. The avalanche terminated at time t_0+4. The ROI represented in gray that was activated at time t_0+1 did not participate in an avalanche, since it did not belong to any activity cluster. For this schematic example the size and duration of the avalanche were equal to S = 72 (the cumulative sum of the number of activated ROIs during the avalanche) and T = 5 × dt (number of frames multiply by the temporal resolution, dt, of the data), respectively. The time-course of the avalanche size, $S(t)$, is shown in the left bottom panel.

Supplemental figure S4. Avalanches at the population level and the effect of coarse graining on avalanche exponents. Related to Figure 2. A-C: We analyzed the neuronal avalanches' statistics after pooling the avalanche sizes and durations of all datasets. For each dataset, sizes were normalized by the total number of cells (N). **A:** Distribution of avalanche durations T (in sec). **B:** Distribution of avalanche normalized sizes S/N. **C:** Relation between $<S/N>$ and T. In (A), (B), and (C) open symbols correspond to time-shuffled datasets and the black dashed lines indicate the expected power-law distributions in the case of a critical behavior. The measured exponents are indicated in each panel. **D-F:** Spatial coarse graining. Co-active ROIs were grouped to form 3D clusters if their Euclidean distance was shorter than a given value R, representing the level of coarse graining. For simplicity, only a 2D scheme is shown. The exponents of the neuronal avalanche obtained for different levels of coarse graining. Note that for clusters larger than a sphere of radius R~30 µm the values of the avalanche exponents deviate from the theoretical values and the exponent relation did not hold anymore (for R<30 µm the variable $q = (\tau - 1)/[\sigma\nu z(\alpha - 1)]$ is close to 1 on average but becomes ≤0.71 for larger radii). The size of the clustering neighborhood used in the present study lies below this threshold. **G-I:** Temporal coarse graining. Avalanche exponents were calculating after down-sampling the data, using time bins equal to 2×dt (E) 3×dt (G), and 4×dt (I), where dt is the original temporal resolution of the data (dt = 0.47 sec). The average variable q is also presented. For time bins longer than 4×dt the values of the avalanche exponents deviate from the theoretical values and the exponent relation did not hold anymore.

Supplemental figure S5. Single anatomical brain regions also show critical dynamics. Related to Figure 6. Neuronal avalanches observed within two brain regions with different functional roles, i.e, the optic tectum (sensory processing) and the rhombomere 7 (reticulospinal circuit for movement generation). **A-C:** Avalanche durations and sizes displayed power-law statistics with power exponents close to the corresponding critical values. Nevertheless, while durations and average sizes of neuronal avalanches in the optic tectum matched the expected scaling relation ($\langle S \rangle(T) \sim T^{1/\sigma\nu z}$, with $\sigma\nu z \approx 0.57$), reticulospinal avalanches deviated from it: for a given duration T, the average size of the avalanches were larger than predicted by criticality theory. **D:** Locations of the optic tectum (blue) and the rhombomere 7 containing the reticulospinal circuit (red) in one optical coronal plane. **E:** Average power-law exponents describing the distribution of durations (α), sizes (τ), and the relation between sizes and durations ($1/\sigma\nu z$) of spontaneous neuronal avalanches displayed in the optic tectum (blue) and the reticulospinal region (red). For comparison, the gray and the black bars indicate the critical exponents of 3D random field Ising theoretical models and the exponents observed in the whole-brain activity, respectively. Differences between whole-brain, optic tectum, and reticulospinal activities were evaluated using ANOVA followed by Tukey-Kramer multiple comparisons tests.
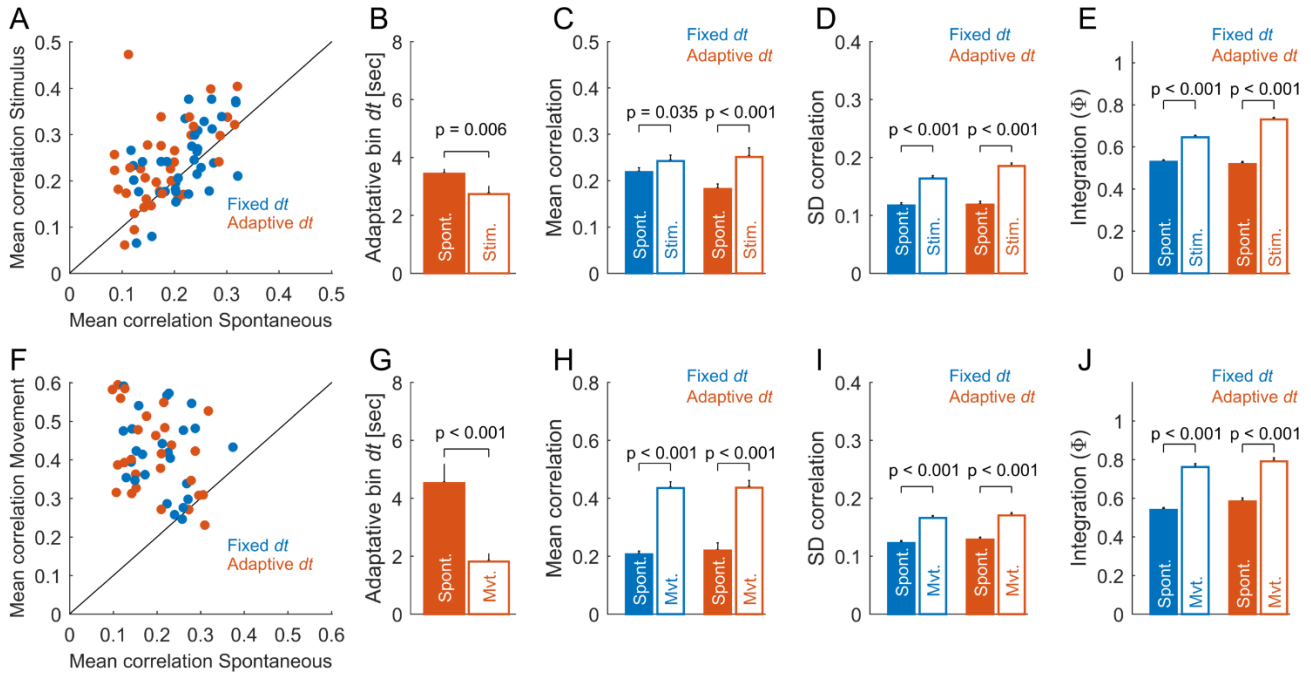
Supplemental figure S6. Activity during sensory stimulation and self-generated behavior presents changes not only in the rate of calcium events but also in their correlation structure. Related to Figure 7. We compared the rate and Pearson correlations of binary data during spontaneous activity, during sensory stimulation, and around spontaneous movements. We also analyzed the data using *adaptive binning*, i.e., by choosing a time bin dt according to the inverse of the average rate of the calcium point processes (Yu et al., 2017). Data with high rate led to a short dt, data with low rate led to a long dt. **A:** Average correlations during spontaneous activity and during sensory stimulation, for fixed dt (equal to a recording frame) and for an adaptive binning. Each dot represents the average correlation in one of the Q data segments, for a given larva. Correlations were calculated for all pairs among 40,000 ROIs. **B:** Adaptive binning for spontaneous and stimulus-induced activities. **C:** Average correlations during spontaneous and stimulus-induced activities, for both types of temporal binning. **D:** Standard deviation of the distribution of correlations during spontaneous and stimulus-induced activities, for both types of temporal binning. **E:** To characterize the topology of the correlation matrices during spontaneous and stimulus-induced activities, we calculated the integration measure, Φ, that quantifies the connectiveness of the matrix (Deco et al., 2015). Briefly, Φ is calculated by, first, thresholding the correlation matrix, making it a binary graph, using a threshold θ. Second, we calculated the largest connected component $LCC(\theta)$ of the binary graph. Finally, Φ is given by the integral of $LCC(\theta)/N$ over all tested thresholds θ, where N is the number of ROIs. p: p-value, two-sample t-test comparing values for spontaneous and stimulus-induced activities. **F-J:** same as panels (A-E) but for data around the onsets of detected tail movements, denoted ton, and compared them to those in the absence of movements. p: p-value, two-sample t-test comparing values around movement onsets and the values in the absence of movements. These results show that sensory stimulation and self-generated behavior change not only the rate of calcium vents but also their correlation level and topology, even in the case of adaptive binning. This shows that the stimulus/movement-induced changes in neuronal avalanche exponents that we observed (**Figure 7**) were not simply explained by a change in the rate of the point process.

A

B

C
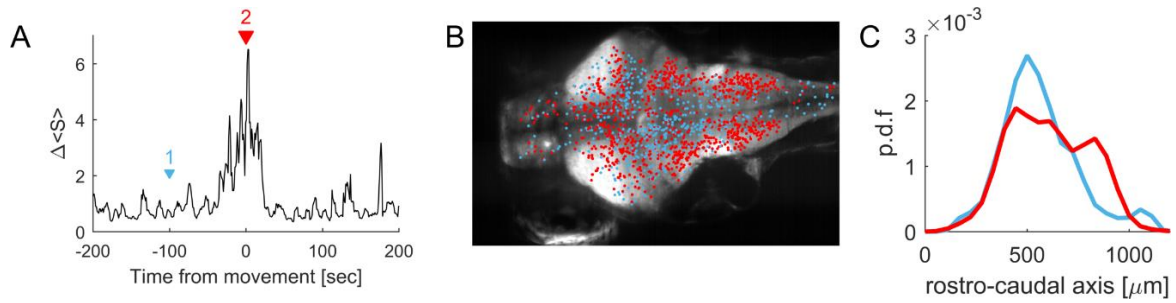
Supplemental figure S7. Neuronal avalanches during self-generated behavior had larger sizes and their distribution across different brain regions was biased towards hind-brain motor areas. Related to Figure 7. A: The average size of neuronal avalanches around self-generated tail movements (0 sec represents the onset of the movement). The values were normalized by the average across time, i.e., $\Delta S = \langle S(t) \rangle_{tails} T / \sum_{t=-200}^{t=+200} \langle S(t) \rangle_{tails}$, where $\langle . \rangle_{tails}$ represents the average over tail movements and T is the length of the observation window. **B:** Locations of the initial centers of mass of neuronal avalanches projected on the coronal (x–y) plane of the brain during periods of spontaneous activity (blue dots, corresponding to the blue epoch in panel A, 1) and during the onset of tail movements (red dots; corresponding to the red epoch in panel A, 2). Each dot represents a neuronal avalanche. **C:** Probability density function of avalanche origins along the rostro-caudal axis during periods of spontaneous activity (blue) and during the onset of tail movements (red). We observed that with respect to periods of spontaneous activity, during tail movements, the neuronal avalanches had larger sizes and their distribution across different brain regions was biased towards hind-brain motor areas (caudal).
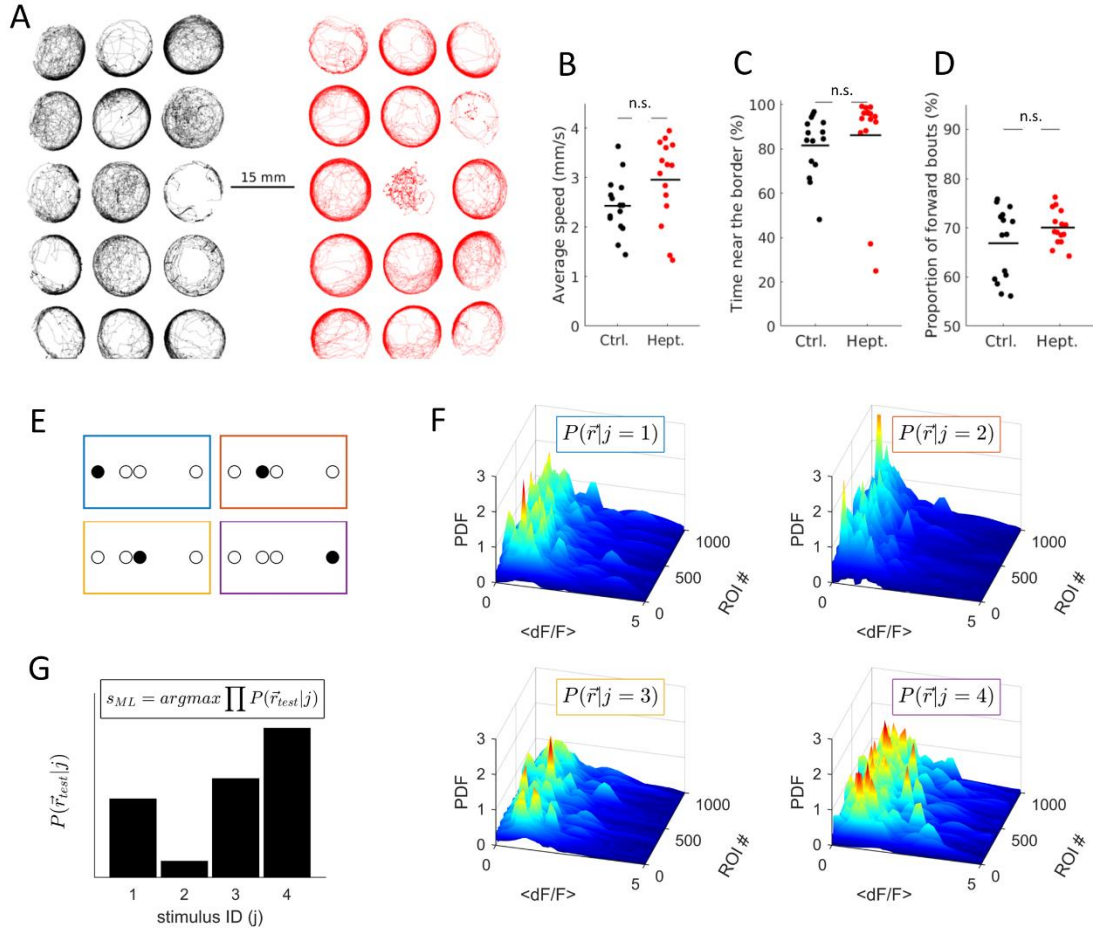
Supplemental figure S8. Effect of heptanol on free-swimming behavior and visual stimulus decoding scheme. Related to Figure 8. We compared the trajectory of 15 freely swimming GCaMP5 larvae at 7 dpf with 15 other GCaMP5 larvae exposed to 90 µM of heptanol for 3 h prior to the experiments. **A:** Paths of the image centroids of each of the 30 larvae in a multi-well plate during 30 min of spontaneous behavior. The paths are colored in black for the control larvae (*left*) and in red for the heptanol exposed larvae (*right*). Note that for visualization purposes only 5 min. of the larvae behavior are shown. **B:** Average speed of the larvae in the control and heptanol-treated conditions. Each dot represents one larva, a horizontal jitter was added for visualization. The horizontal lines represent the mean of the two distributions (Ctrl.: 2.43 ± 0.04 mm/sec vs. Hept.: 2.96 ± 0.06 mm/sec; p=0.054, two-sample t-test). **C:** The time the larvae spent near the border of the recording chamber (< 2mm from the border). The horizontal lines represent the mean of the two distributions (Ctrl.: 81.5 ± 13.6 % vs. Hept.: 86.08 ± 22.77 %; p=0.51, two-sample t-test). **D:** Distribution of the turning behavior quantified by the proportion of forward swimming bouts (a change in direction < 10 deg.). The horizontal lines represent the mean of the two distributions (Ctrl.: 66.85 ± 7.22 % vs. Hept.: 70.03 ± 3.5 %; p=0.14, two-sample t-test). **E-G:** A maximum likelihood decoder (MLD) was used to classify the location of visual stimuli presented to larvae from the fluorescence signals $\Delta F/F$ in the optic tectum. **E:** The stimulus set was composed of light spots of 4 deg. presented at four possible spatial locations (75º, 85º, 90º, 110º). **F:** The neuronal responses of n ROIs, $\vec{r} = [r_1, r_2, …, r_n]$, were used to learn the probability distributions of the response of each ROI to each stimulus of category j, i.e., $P(\vec{r}|j)$. **G:** The MLD chooses the stimulus that is statistically most likely to have elicited a newly observed response of the n signals, i.e., $\vec{r}_{test} = [r_1, r_2, …, r_n]$, given the learned probability distributions. With the simplifying assumption that the responses of the ROIs were assumed to be statistically independent from each other, the decoding of the population response consisted of searching for the stimulus (s_{ML}) which maximized the probability of the testing response: $s_{ML} = argmax \prod_{i=1}^{n} P(r_{i,test}|j)$. The performance was defined as the proportion of population response vectors that were correctly classified.

Supplementary Videos

Supplemental video S1. Whole-brain neuronal activity. Related to Figure 1; Figure 2. The first row displays the relative increase in fluorescence ($\Delta F/F$) in the hexagonal regions of interest (ROIs) in five different coronal sections. The second row shows the corresponding binarized activity used to compute the clusters. The last row depicts the time-course of the percentage of active ROIs in the entire volumetric recording.